

# Neutrino halo effect on collective neutrino oscillation in iron core-collapse supernova model of a $9.6 M_{\odot}$ star

Masamichi Zaizen<sup>1,\*</sup>, John F. Cherry<sup>2</sup>, Tomoya Takiwaki<sup>3</sup>, Shunsaku Horiuchi<sup>4</sup>, Kei Kotake<sup>5,6</sup>, Hideyuki Umeda<sup>1</sup>, and Takashi Yoshida<sup>1</sup>

<sup>1</sup>*Department of Astronomy, Graduate School of Science, University of Tokyo, Tokyo 113-0033, Japan*

<sup>2</sup>*Department of Physics, University of South Dakota, Vermillion, SD 57069, USA*

<sup>3</sup>*Division of Science, National Astronomical Observatory of Japan, 2-21-1 Osawa, Mitaka, Tokyo 181-8588, Japan*

<sup>4</sup>*Center for Neutrino Physics, Department of Physics, Virginia Tech, Blacksburg, VA 24061, USA*

<sup>5</sup>*Department of Applied Physics, Fukuoka University, Nanakuma 8-19-1, Johnan, Fukuoka 814-0180, Japan*

<sup>6</sup>*Research Institute of Stellar Explosive Phenomena, Fukuoka University, Nanakuma 8-19-1, Johnan, Fukuoka 814-0180, Japan*

(Dated: May 24, 2022)

For the first time within a multi-angle computational framework we investigate the time evolution of neutrino halo effects on collective neutrino oscillation (CNO) in an iron core-collapse supernova. For the collapse of the  $9.6 M_{\odot}$  progenitor employed in this work, we find that there is a window of time where one can safely calculate CNO including the neutrino halo effects due to the density gradient of the envelope. The impact of inward-scattered neutrino flux on CNO can not be ignored inside the shock front, compared with the outward-propagating neutrino flux. However, there is a window of time where CNO is not shut down by multi-angle matter suppression and delayed in onset beyond the radius of the growing shock front. Halo neutrinos with wider intersection trajectories induce a delay for the onset radius of CNO, while they produce additional flavor conversion for neutrino spectra. This additional flavor conversion sharpens CNO spectral features, leading to a detected neutrino signal which is more clearly distinguishable from thermal emission than when halo neutrinos are omitted.

PACS numbers: 14.60.Pq, 95.85.Ry, 97.60.Bw

## I. INTRODUCTION

Neutrinos are intensively emitted from supernovae and have the potential to carry with them information on the central properties of the explosion [1–8]. Kamiokande-II and Irvine-Michigan-Brookhaven detector detected eleven and eight neutrinos, respectively, from SN1987A which emerged in the Large Magellanic Cloud [9, 10]. This observation indicated the importance of neutrinos in core-collapse supernovae (CCSNe) [11]. However, there are still many open questions in supernova physics. We do not completely understand what happens in the core of exploding stars. Central densities are sufficient to trap even neutrinos, which then diffuse and are emitted from the proto-neutron star at the core. The energy spectra for different lepton flavors of neutrinos depend sensitively on the equation of state of nuclear matter in the emission region. More precise models of neutrino emission and flavor transformation enable us to enrich our understanding of CCSNe. Current and future neutrino detectors expect that several thousands of neutrino events may be observed from a galactic signal (e.g., [12]). In this case, we will obtain detailed time evolution of the neutrino spectra. This information is expected to reveal many properties inside CCSNe and, hopefully, enable us to test our current understanding of the yet-uncertain

supernova physics (e.g., [13]).

However, we can not get original neutrino spectra directly from observation without accounting for neutrino oscillations. Neutrinos from CCSNe undergo flavor conversions and mixed states arrive at the Earth [14–16]. First, neutrino oscillation in vacuum is a  $SU(3)$  oscillator system typically parameterized by two mass-squared differences, three mixing angles, and a complex phase. With the exception of the complex phase, these parameters are currently well-known thanks to the hard work of many neutrino experiments (see summary in Ref. [17]). Furthermore, neutrinos undergo flavor conversion with background matter described by the Mikheyev-Smirnov-Wolfenstein (MSW) effect which occurs at two typical electron densities [18, 19]. These two types of neutrino oscillation are linear effects and can easily be grasped in solar and atmospheric neutrino probes. On the other hand, a third phenomenon becomes potentially dominant in CCSNe which is triggered by neutrino-neutrino coherent forward scattering interactions in the high neutrino flux regions near the proto-neutron star. Known as collective neutrino oscillation (CNO), neutrinos propagating on intersecting trajectories develop quantum coherence in their flavor oscillation with adjacent neutrinos. While this process has been studied intensively for more than a decade, the non-linear nature of the phenomenon makes the outcome of flavor oscillation impossible to predict without computational modeling. One of the known outcomes of CNO is a peculiar behavior, called a spectral split or swap, where the neutrino spectra exhibit flavor

\* mzaizen@astron.s.u-tokyo.ac.jp

exchange only above a critical energy; this behavior is not seen in linear effects [20].

The neutrino-neutrino coherent forward scattering interaction depends strongly on the relative trajectories of intersecting neutrinos. Treatment of CNO often employs the multi-angle approximation, which considers polar angular distributions of emitted neutrinos in detail. Neutrinos along different trajectories are forced to synchronize into coherent oscillation modes by the self-interactions and maintain coherence among different angular paths. On the other hand, this trajectory dependence enhances matter-induced decoherence. Background electrons cause the phase dispersion due to the travel distance difference. This phenomenon is called multi-angle matter suppression, and it weakens CNO [21]. It does not occur under the single-angle approximation which ignores angular dependence of neutrino wave function. The competition between the neutrino self-interaction and the matter-induced phase dispersion is important under realistic supernova environments [22–25].

These interesting features are based on the “bulb model”, which imposes many assumptions on neutrino emissions and background environments. Recent studies have revealed that symmetry breaking can enhance new behaviors of CNO [26–38]. Some of these instabilities can overcome the multi-angle matter suppression and may have large influence on observed neutrino spectra. However, few detailed calculations using realistic supernova models have been performed due to the numerical complexity.

Many groups have extended the bulb model and tackled CNO. For example, Cherry *et al.* suggested that some of the neutrinos experience a direction-changing scattering with nucleon/nucleus outside the neutrino sphere [26, 27]. These scattered neutrinos produce a “halo” flux of neutrinos with large intersection angles with outgoing neutrinos and may have a large impact on the neutrino-neutrino interaction. Especially, the authors pointed out that inwardly scattered neutrinos can destroy the bulb framework and produce numerical obstacles under some circumstances. The inward-going flux depends on the background matter density and composition, integrated over the interior of the entire CCSN envelope. The previous work employed an electron capture CCSN model whose density profile steeply drops at  $r > 1000$  km. Thus, the inward halo flux decreases outside the steep density gradient, and CNO with bulb+halo model was able to be performed safely. Ref. [28] investigated including the inward-scattered neutrinos self-consistently within simplified CNO calculations. The authors showed that main features in CNO with single-angle approximation, which averages neutrino states with different angular modes, are maintained under the inclusion halo flux by searching for a relaxation solution under the assumption of a static total neutrino flux.

In this paper we perform the first ever study of CNO in an iron-CCSNe which includes the halo flux in a multi-

angle solution framework. For completeness we compare the results of our full calculation (“with halo”), one which omits halo neutrinos scattering (“no halo”), and the results of neutrino emission which omits CNO entirely (“no CNO”) in order to evaluate the time evolution of the signal and the event rates observed by neutrino detectors. Our principle finding is that the presence of the halo neutrinos enhances the detectability of CNO spectral features.

In section II, we introduce our calculation method and employed supernova model. We present the results of halo distribution, flavor conversions, and detectability in section III. Finally we summarize the conclusions of our study in section IV.

## II. NUMERICAL SETUP

### A. Supernova model

We perform a two-dimensional (axi-symmetric) CCSN simulation with a  $9.6 M_{\odot}$  zero-metallicity model (Z9.6) provided by A. Heger (2017, private communication, this model is an extension of Heger *et al.* 2010 [39] toward the lower mass). This progenitor is a non-rotating star and has an iron-core in the center, different from O-Ne-Mg progenitor used in previous work [27].

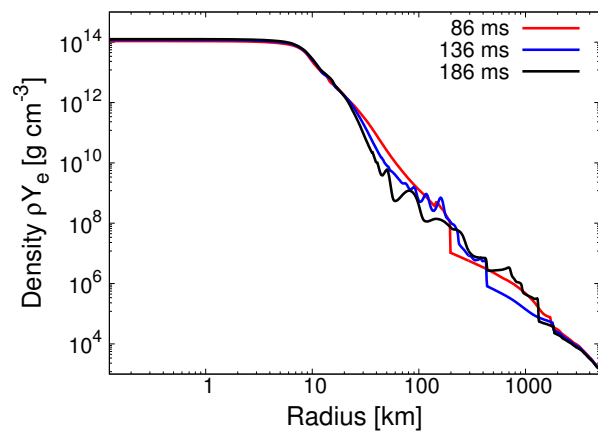


FIG. 1. Electron density profile along the north pole at post-bounce time  $t_{\text{pb}} = 86, 136,$  and  $186$  ms. Shock wave propagates from 200 km to 1000 km.

The hydrodynamical simulation is performed by 3DnSNe code (recent application reference [40, 41]), and we show a selection of results for the electron density profile along the north polar direction at 86 ms, 136 ms, and 186 ms in Figure 1. This two-dimensional simulation is computed on a spherical polar coordinate with spatial resolution of  $(N_r, N_{\theta}) = (512, 128)$ . This radial grid covers from the center to an outer boundary of 5000 km. A piecewise linear method with geometrical correction is used to reconstruct variables at the cell edge, where a modified van Leer limiter is employed to satisfy the

condition of total variation diminishing (TVD) [42]. The numerical flux is calculated by HLLC solver [43]. We adopt the equation of state by Lattimer & Swesty with incompressibility of  $K = 220$  MeV [44].

Figure 2 represents the time evolution of neutrino luminosities  $L_\nu$ , averaged neutrino energies  $\langle E_\nu \rangle$ , rms energy  $\sqrt{\langle E_\nu^2 \rangle}$ , and shock radius. In these neutrino properties,  $\nu_X$  means nonelectron type neutrinos  $\nu_\mu, \bar{\nu}_\mu, \nu_\tau$ , and  $\bar{\nu}_\tau$ . We approximate neutrino spectra on the surface of neutrino sphere by a gamma distribution [45–47]:

$$f(E_\nu) = \frac{\langle E_\nu \rangle^\xi}{\Gamma_{\xi+1}} \left( \frac{\xi+1}{\langle E_\nu \rangle} \right)^{\xi+1} \exp \left[ -\frac{(\xi+1)E_\nu}{\langle E_\nu \rangle} \right], \quad (1)$$

where  $\Gamma_{\xi+1}$  is the Gamma function. This  $\xi$  is a pinching parameter given by

$$\xi = \frac{\langle E_\nu^2 \rangle - 2\langle E_\nu \rangle^2}{\langle E_\nu \rangle^2 - \langle E_\nu \rangle^2}. \quad (2)$$

This shock radius also shows the evolution of multi-dimensionality. The radius of shock wave is almost spherically symmetric before  $t_{\text{pb}} \sim 100$  ms (with  $t_{\text{pb}}$  the post-bounce time) while two dimensionality evolves and difference between maximum and minimum shock radius emerges after  $t_{\text{pb}} \sim 100$  ms.

## B. Collective neutrino oscillation

The flavor conversions including CNO are performed by using the bulb model as a starting point [20, 48, 49], and extending the formalism to include halo neutrinos [27]. The traditional bulb model requires uniform and isotropic neutrino emissions under environments depending only on radius  $r$ . Neutrino states are simply given by a density matrix  $\rho(r; E, \theta)$  with neutrino energy  $E$  and angular mode  $\theta$  at a radius  $r$ . Equations of motion for a density matrix  $\rho_\nu$  in a steady state are

$$i\partial_r \rho_\nu = [H_{E,u}, \rho_\nu] \quad (3)$$

$$H_{E,u} = \frac{1}{v_{r,u}} \left( U \frac{M^2}{2E} U^\dagger + \sqrt{2} G_F n_e L \right) + \frac{\sqrt{2} G_F}{4\pi r^2} \int dE' du' \left( \frac{1}{v_{r,u} v_{r,u'}} - 1 \right) (\rho'_\nu - \bar{\rho}'_\nu), \quad (4)$$

where  $U$  is the Pontecorvo-Maki-Nakagawa-Sakata matrix [50],  $M^2$  is a neutrino mass square matrix,  $G_F$  is the Fermi coupling constant, and  $L$  is  $\text{diag}(1, 0, 0)$ . The radial velocity  $v_{r,u}$  with an angular mode  $u$  is defined as

$$v_{r,u} = \sqrt{1 - u \frac{R_\nu^2}{r^2}} \quad (5)$$

$$u = \sin^2 \theta_R, \quad (6)$$

where  $\theta_R$  is an emission angle relative to the radial direction at the neutrino sphere. We assume axial symmetry on the neutrino trajectories, that is, we neglect the multi-azimuthal angle effect [29]. This symmetry

breaking appears only in the normal mass ordering and the directional azimuth-angle distribution does not affect the flavor conversions in the inverted mass ordering [31, 34, 51]. We describe the flavor difference with polarization vectors  $\mathbf{P}$  and  $\bar{\mathbf{P}}$  in solving the equation of motion numerically. This three-flavor formalism is based on Ref. [25, 49]. We calculate CNO along the northern pole direction of the two-dimensional iron-CCSN model.

In this work, we choose the following neutrino parameters as in Ref. [17]:  $\Delta m_{21}^2 = 7.37 \times 10^{-5} \text{ eV}^2$ ,  $|\Delta m_{31}^2| = 2.54 \times 10^{-3} \text{ eV}^2$ ,  $\sin^2 \theta_{12} = 0.297$ ,  $\sin^2 \theta_{13} = 0.0216$ , and CP-violation phase  $\delta = 0$ . We consider only the inverted mass ordering case  $\Delta m_{31}^2 < 0$  because CNO is suppressed for the normal mass ordering case in our calculations. We introduce the rotated state,

$$\nu_x = \cos \theta_{23} \nu_\mu - \sin \theta_{23} \nu_\tau \quad (7)$$

$$\nu_y = \sin \theta_{23} \nu_\mu + \cos \theta_{23} \nu_\tau, \quad (8)$$

not the ordinary state  $(\nu_e, \nu_\mu, \nu_\tau)$  in the following calculations. This rotation does not affect the electron-type neutrinos, and enables us to understand the three-flavor framework as the combination of two-flavor problems,  $\nu_e \leftrightarrow \nu_y$  and  $\nu_e \leftrightarrow \nu_x$ . The three-flavor effects associated with  $\Delta m_{21}^2$  and  $\theta_{12}$  arise from flavor symmetry condition on the total neutrinos fluxes for each flavor,  $\Phi_\alpha = L_{\nu_\alpha} / \langle E_{\nu_\alpha} \rangle$ , such that  $\Phi_{\nu_e} \simeq \Phi_{\bar{\nu}_e} \simeq \Phi_{\nu_x}$ , and cause  $\nu_e \leftrightarrow \nu_x$  conversion [51–53]. These effect can emerge even in the normal mass ordering, but neutrino number fluxes in Figure 2 do not satisfy the symmetry condition. Therefore,  $\nu_e \leftrightarrow \nu_y$  conversion is dominant in our calculation.

## C. Neutrino halo

Inclusion of the neutrino halo effect within the framework of CNO calculations has received a renewed burst of attention [28, 54] due, in part, to the recent direct detection of coherent enhancement of elastic neutrino-nucleus scattering by the COHERENT experiment [55]. This result has placed the presence of the neutrino halo within CCSNe on firmer theoretical ground than CNO itself, as  $\nu - \nu$  coherent forward scattering has not yet been directly observed.

The enhanced neutrino-nucleus interaction cross section, first calculated by Tubbs and Schramm [56], is isotropic and thus responsible for redirecting a portion of the neutrino flux emitted during a CCSN along all trajectories within the envelope of the exploding star. The magnitude of the population of halo neutrinos created by this scattering process is  $\propto A$ , the nuclear mass number of nuclei within the envelope, which is in turn due to the  $\propto A^2$  scaling of the coherently enhanced cross section combined with the  $\propto A^{-1}$  scaling of the density of atomic nuclei. For CCSNe which arise from iron-core progenitor stars (estimated to be  $\sim 70\%$  of the galactic population [57]), the magnitude of the halo effect is proportionately larger than the previously studied O-Ne-Mg

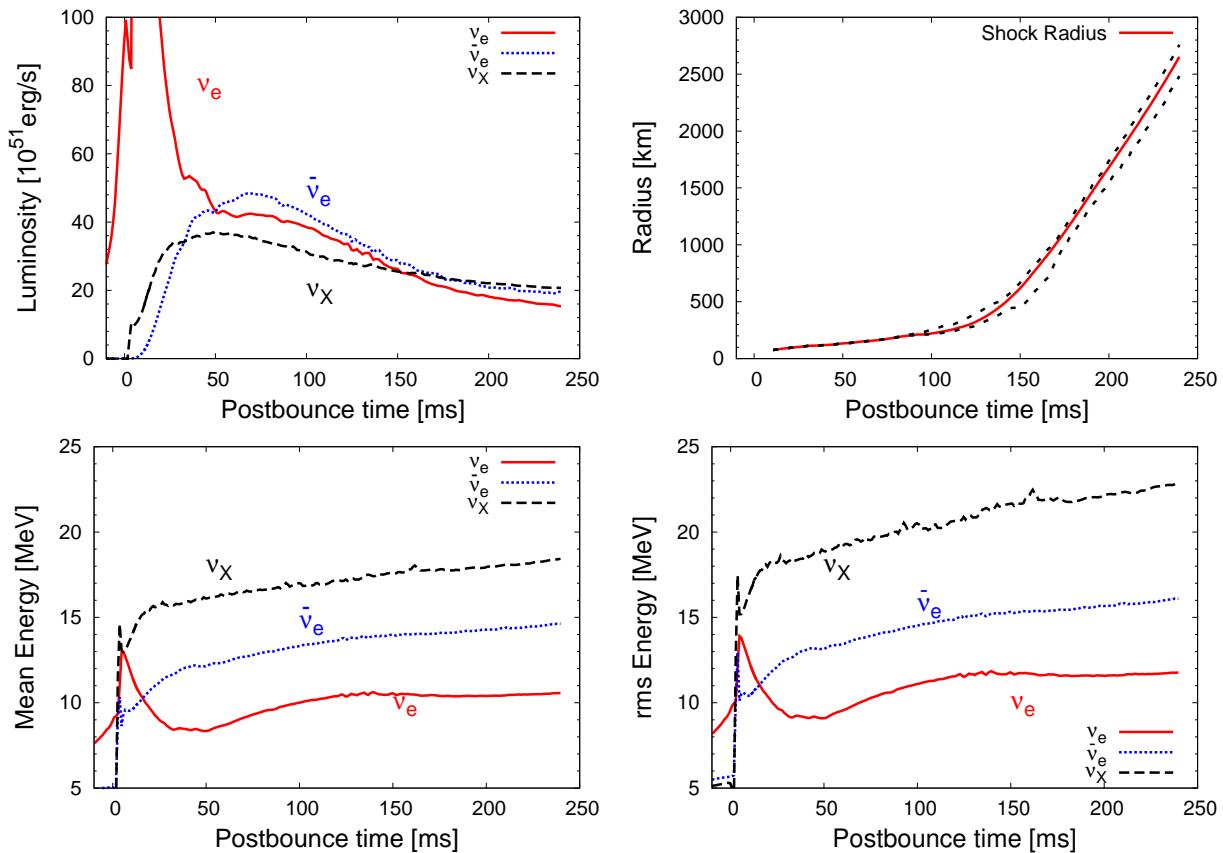


FIG. 2. The top panels show the time evolution of neutrino luminosity (left) and shock wave radius (right). In the bottom panels, we show averaged energy (left) and rms energy (right). In neutrino luminosity and average energy,  $\nu_e$ ,  $\bar{\nu}_e$ , and  $\nu_X$  are red solid, blue dotted, and black dashed line, respectively. For the shock radius figure, dotted lines show the maximum and minimum radius.

core collapse case. To accommodate the increased magnitude of the halo effect for the Z9.6 CCSN simulation, we have adapted the approach of [27] to include a thorough set of safety checks prior to conducting a full CNO calculation.

To begin with we define the quantities,

$$H_{\nu\nu}^{\text{out}} = \Sigma_{\alpha} \sqrt{2} G_{\text{F}} \int_0^{\pi/2} (1 - \cos \theta) [\rho_{\nu_{\alpha}}(\theta) - \bar{\rho}_{\nu_{\alpha}}(\theta)] d\theta, \quad (9)$$

and

$$H_{\nu\nu}^{\text{in}} = \Sigma_{\alpha} \sqrt{2} G_{\text{F}} \int_{\pi/2}^{\pi} (1 - \cos \theta) [\rho_{\nu_{\alpha}}(\theta) - \bar{\rho}_{\nu_{\alpha}}(\theta)] d\theta, \quad (10)$$

which are the  $\nu - \nu$  Hamiltonian contributions for a radially directed neutrino from outward directed neutrinos and inward directed neutrinos, respectively. Equations (9) and (10) can be evaluated explicitly under the assumption that the neutrino density matrices  $\rho_{\nu}$  and  $\bar{\rho}_{\nu}$  are flavor diagonal, i.e. in the absence of neutrino flavor transformation, for all points within the CCSN envelope. With these constructions we can quantify the amount of  $\nu - \nu$  flavor transformation Hamiltonian “weight” which is flowing inward vs. outward. This is a critical step in

implementing multi-angle CNO with the inclusion of the halo population [27], as inward directed neutrinos cannot be accommodated by the numerical methods presently available (although considerable progress has been made toward rectifying this issue for single-angle CNO calculations [28, 54]).

To create a quantitative metric on the suitability of our multi-angle CNO calculations, we require that the ratio  $H^{\text{in}}/H^{\text{out}}$  be less than 10% at all radii along which we solve Equation (3). This guarantees that the portion of the halo population which cannot be included in the multi-angle CNO calculations is, at most, a sub-leading order contribution to  $H_{\text{E,u}}$ . Mapping the ratio  $H^{\text{in}}/H^{\text{out}}$  for all points within the envelope is the first step in our safety checks.

The second step is to check that the flavor diagonal condition used in evaluating Equations (9) and (10) is valid up to the radius at which we begin the CNO calculation. Beneficially, the large matter densities in the inner regions of the CCSN envelope suppress neutrino flavor conversion at small radii. To establish the maximum radius at which we can perform our full CNO calculation, we perform a CNO calculation which omits the halo neutrinos. The results of this calculation are suffi-

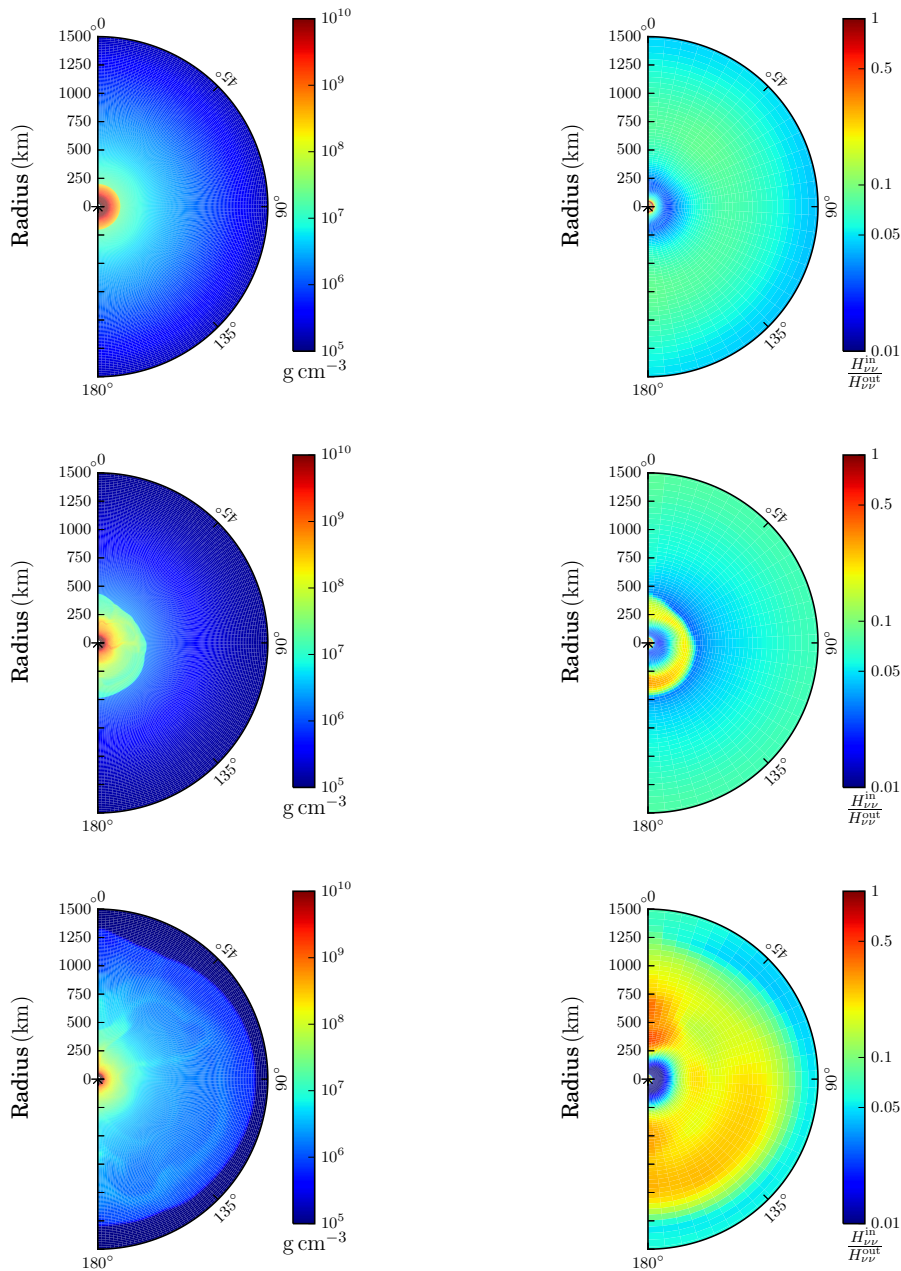


FIG. 3. Density profile (left) and Halo contribution (right). These figures show three time snapshots, postbounce time 86 ms, 136 ms, and 186 ms, from top to bottom. Color scale for the right panels indicates the ratio of the self-interaction Hamiltonian of inward contribution to outward one. A region where this ratio exceeds 0.1 should not be treated by the bulb+halo model. A movie presenting the time evolution is available at <http://tron.astron.s.u-tokyo.ac.jp/~zaizen/halo-movie.html>

cient to establish the initial radius,  $r_{\text{init}}$ , below which the flavor diagonal assumption is valid due to matter density suppression of CNO.

The final preparatory step we take is to verify that both of the above conditions are satisfied simultaneously along the trajectory where we calculate CNO. While the ratio  $H^{\text{in}}/H^{\text{out}}$  may grow larger than 10% at some radii along a given trajectory, so long as those locations are within the region of matter suppression of CNO we con-

sider the effects of the halo neutrino population on flavor conversion to be negligible. Under the condition that  $H^{\text{in}}/H^{\text{out}} < 10\%$  at all radii greater than  $r_{\text{init}}$  we consider a trajectory safe for the full calculation of CNO including all radially emitted neutrinos and outward directed halo neutrinos.

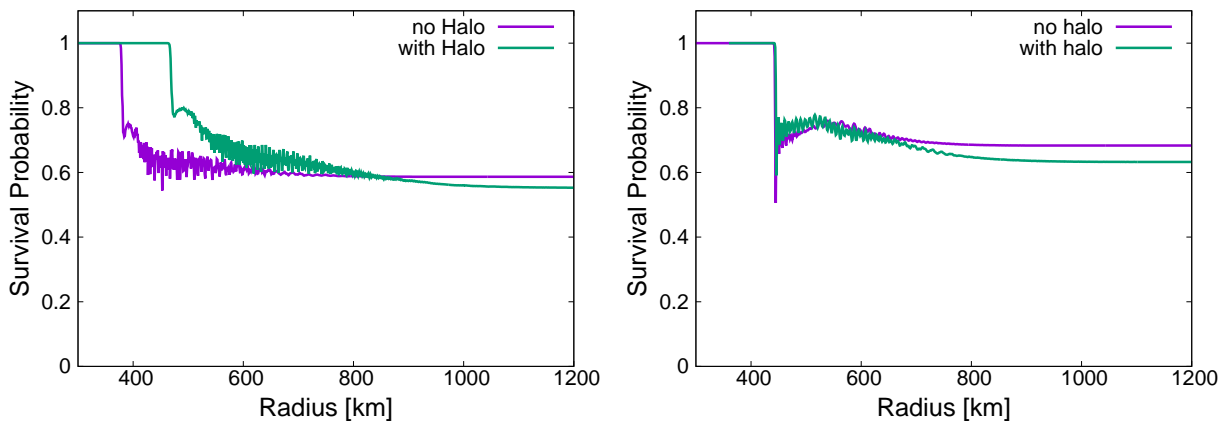


FIG. 4. The radial evolution of the energy and angle averaged  $\nu_e$  survival probability at postbounce time 86 ms (left) and 136 ms (right). These survival probabilities are in the inverted mass ordering case.

### III. RESULTS

#### A. Magnitude of Halo

We show density profile and halo contribution at 86 ms, 136 ms, and 186 ms in Figure 3.

This halo contribution expresses the ratio  $H^{\text{in}}/H^{\text{out}}$  of the self-interaction Hamiltonian of inward contribution to outward one. We can not neglect inward-scattered neutrino flux in a region where this ratio exceeds 10%. This dangerous region especially expands over the whole map at 186 ms. However, we find an escape route along 45 degree direction. This gap is produced by two-dimensional density structure and neutrino flux distribution.

Comparing this region with the density profile, we find that the halo contribution is larger inside the shock wave and it steeply becomes smaller outside it. This feature is similar to the steep density gradient in a O-Ne-Mg CCSN. Therefore, the density gradient of the shock wave has the same effect as the envelope density gradient in O-Ne-Mg CCSNe. We can calculate CNO safely, ignoring inward-going neutrino flux outside the shock wave. In this case, we replace the neutrino sphere  $R_\nu$  with a neutrino-halo sphere  $R_H$  as an emission source. The radius of neutrino-halo sphere almost corresponds to the shock wave location and the flavor conversion does not occur inside this neutrino-halo sphere. Using this bulb+halo model, we investigate the impacts of outward-going neutrino flux on CNO signals.

#### B. Halo effects on flavor conversion

In our model, the shock wave propagates outward within the occurrence region of CNO. This propagation varies the density structure in this region as time passes, and the behaviors of the multi-angle matter suppression change. We show the time variation of density profile along the north polar direction at 86 ms, 136 ms, and

186 ms in Figure 1. CNO at 186 ms is completely suppressed due to matter effects. We first show results at 86 ms and 136 ms. Figure 4 shows the radial evolution of the survival probability of electron neutrinos averaged over energy and angular mode at 86 ms and 136 ms. At 86 ms, the shock wave is located at  $r \sim 200$  km and CNO occurs outside the shock wave in the no-halo case. The electron density gradually decreases with increasing radius, and flavor conversions occur at  $r \sim 400$  km.

In the with-halo case, the onset of flavor conversion is clearly delayed. The with-halo case suggests that the neutrino halo gives additional multi-angle matter suppression for CNO. The matter suppression is induced by the phase dispersion due to the different neutrino trajectories. The maximum value of intersection angle in the no-halo case depends roughly on the inverse square of the radius at a distance  $r \gg R_\nu$ . On the other hand, halo components have broader angle distribution and give additional phase dispersion. Halo neutrinos with wide angles strengthen the multi-angle matter suppression, and the onset radius of CNO is delayed.

At 136 ms, there is no difference between oscillation radius in the no-halo case and the with-halo case. The shock wave is located at  $r \sim 430$  km at this time snapshot. Neutrinos get free from the matter suppression just after propagating through the shock wave, and CNO suddenly occurs. This feature does not change even in the with-halo case. Therefore, the onset radius of CNO is same as in the no-halo case, different from at 86 ms.

Second, we present calculation results of CNO in the no-halo case and the with-halo case at 136 ms as a representative snapshot. Figure 5 shows the survival probability contour maps on energy-impact parameter plane after the CNO ceases at  $r = 1200$  km.

The left panels in Figure 5 are results in the no-halo case and the right ones are in the with-halo case. The top panels show the results for ordinary neutrinos and the bottom ones are for antineutrinos. The vertical axis expresses the impact parameter  $b = r \sin \theta_R$  of emitted neutrinos from neutrino sphere/neutrino-halo sphere

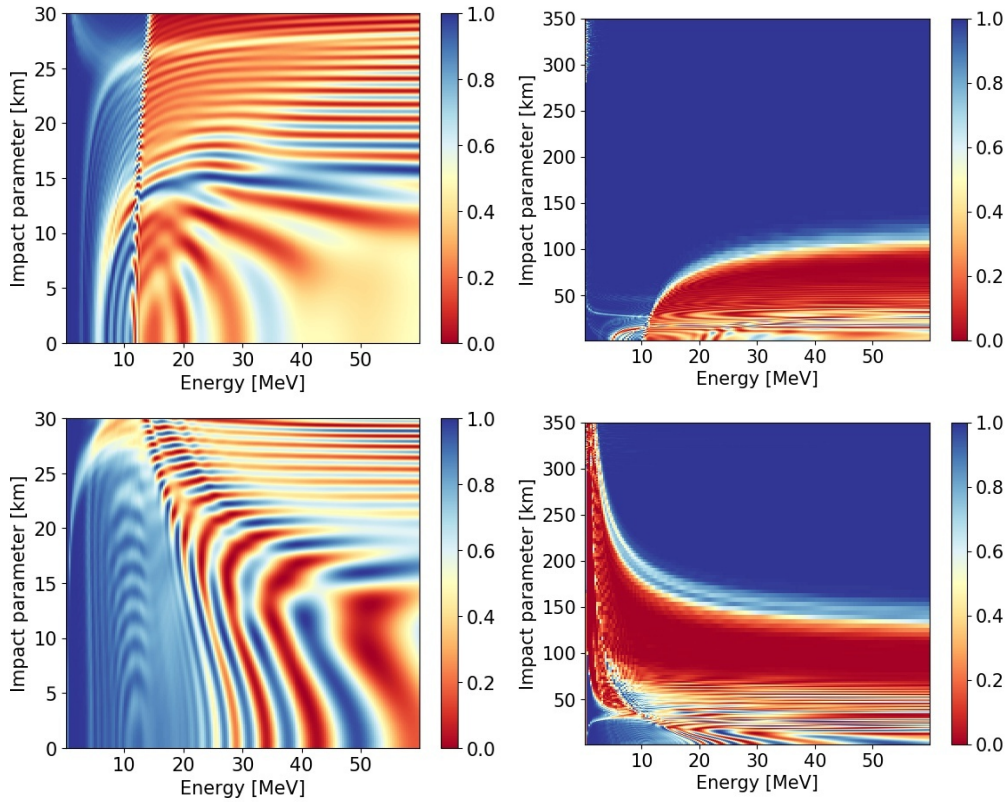


FIG. 5. The survival probability contour maps for neutrinos (upper panels) and antineutrinos (bottom panels) on energy-impact parameter plane at  $r = 1200$  km at postbounce time 136 ms. Left panels are the no-halo case and right panels are the with-halo case.

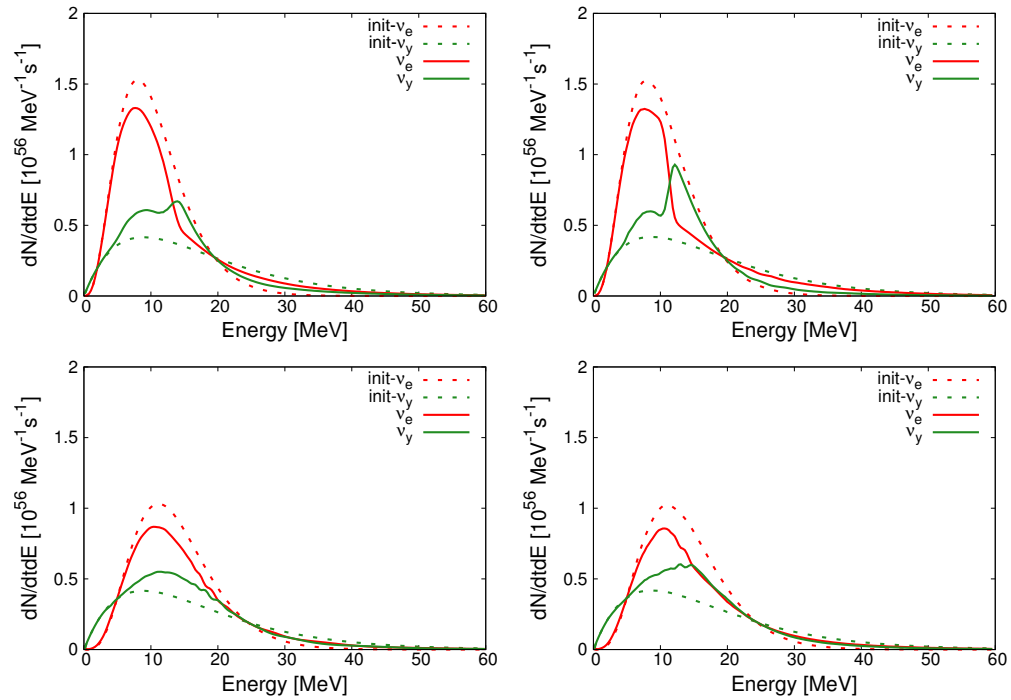


FIG. 6. Neutrino spectra (upper panels) and antineutrino spectra (bottom panels) after the CNO ceases at  $r = 1200$  km at postbounce time 136 ms. Left panels are the no-halo case and right panels are the with-halo case. The  $e$  and  $y$  flavors are shown in red and green lines, respectively. The solid lines are for neutrino spectra after CNO and the dashed ones for initial spectra.

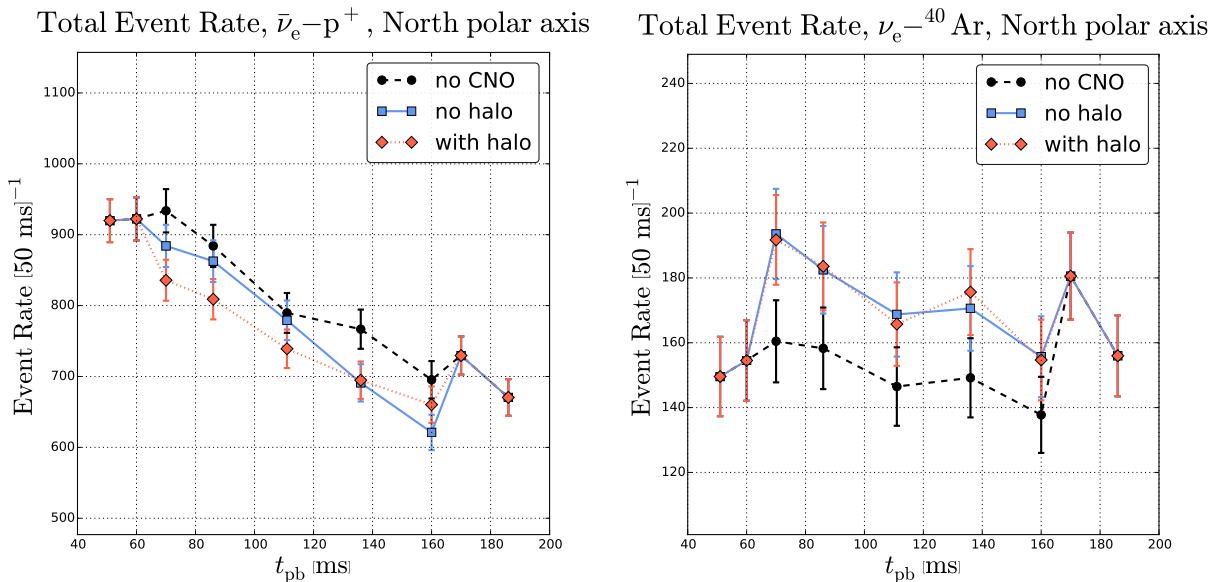


FIG. 7. Left panel: the time evolution of the inverse beta decay event rate at Super-Kamiokande. Right panel: the time evolution of the electron neutrino- ${}^{40}\text{Ar}$  capture rate at DUNE.

which terminates at  $r = R_H$ . Emissions with impact parameter beyond the radius of proto-neutron star, 30 km, correspond to the contribution from neutrino halo. The survival probabilities for neutrinos in the no-halo case clearly predict spectral splits as shown in the previous works [58]. In the with-halo case, halo contributions give additional flavor conversions above the low impact parameter region. These additional oscillations deform the neutrino spectra and affect the detection at the Earth.

Figure 6 shows the angle-averaged neutrino spectra after CNO ceases at  $r = 1200$  km. Left panels are the no-halo case and right panels are the with-halo case. Additional flavor conversion above  $\sim 10$  MeV occurs, in both neutrinos and antineutrinos. This feature corresponds to the survival probability contour map in Figure 5. However, it does not appear to match over low energy range below  $\sim 10$  MeV for antineutrinos. Halo components in this region show almost complete flavor conversions. This shift in the flavor transformation pattern is due to the redistribution of halo neutrinos to wider angles.

### C. Detectability

We find that multi-angle matter suppression prevents CNO at early and late times, with the exception of a window from  $t_{\text{pb}} = 70$  ms to  $t_{\text{pb}} = 170$  ms during the shock revival epoch of the explosion. There are two salient questions we would like to answer with regards to the resultant neutrino signal for the Z9.6 simulation: (1) Can we detect the onset / end of CNO within the received signal? (2) What impact, if any, does the inclusion of the neutrino halo in the CNO calculation have on the received signal?

To address these two questions, we have taken several limiting cases for fluxes of neutrinos generated by our flavor transformation calculations, one including matter effect only (no CNO), one including radially emitted neutrinos only (no halo), and radially emitted neutrinos including the outward directed halo neutrinos (with halo), and used the SNOwGLoBES software package [59] to model the detected signal corresponding to several time snapshots of the explosion. We have chosen to compare event rates for inverse beta-decay (IBD) in Super-Kamiokande (assuming the detector has completed doping with Gd, allowing for the tagging of IBD events), and  $\nu_e - {}^{40}\text{Ar}$  capture in a 40 kt liquid argon (LAr) detector, projected to be similar to the DUNE. Our reasoning behind considering the IBD rate in Super-Kamiokande (SK) rather than the event rate in the proposed Hyper-Kamiokande (HK) detector is driven by our interest in the spectral distortions created by CNO signals. Hyper-Kamiokande will have a fiducial mass of 190 kt of water, compared to Super-Kamiokande's fiducial mass of 22.5 kt, which will dramatically increase the total number of neutrino events observed by HK relative to SK and make HK considerably more sensitive to fast time variations of the SN neutrino burst. However, because the HK detector will not be Gd doped it will not be able to identify IBD events uniquely. The events observed by HK will be a convolution of all neutrino detection channels (both capture and elastic scattering) for all flavors of neutrinos. Because CNO signals are typified by spectral swaps between neutrino flavors a single flavor detection channel is superior in identifying the presence of CNO, so we have elected to examine the SK IBD signal due to its ability to measure  $\bar{\nu}_e$  in isolation. For all analyses we conduct, event rates are calculated fixing the separation

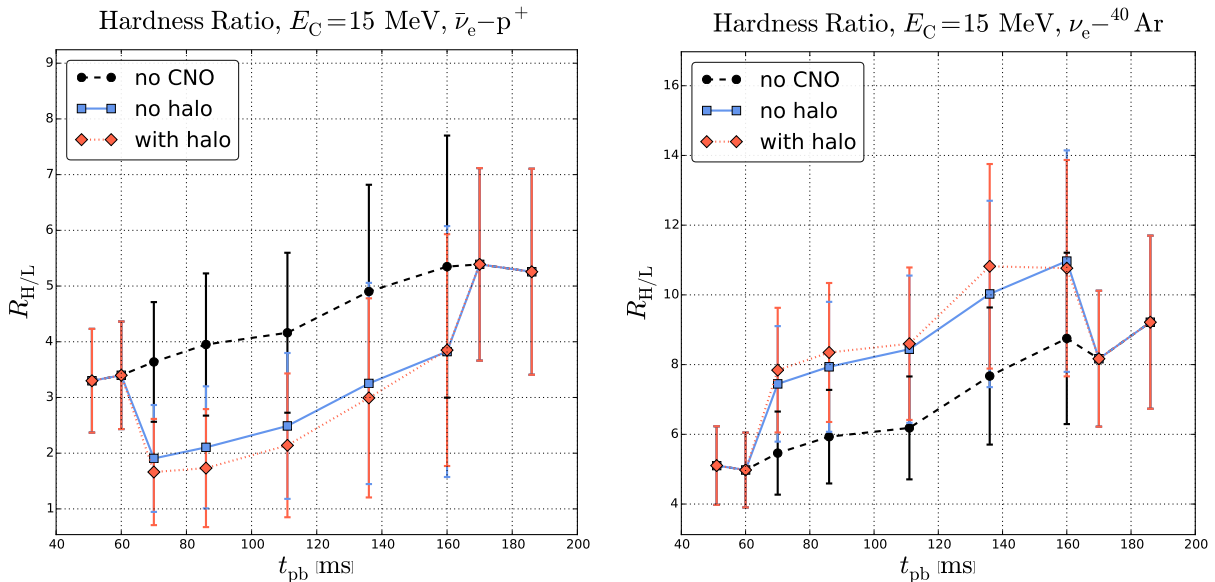


FIG. 8. Left panel: the time evolution of the Hardness ratio,  $R_{H/L}$ , for the inverse beta decay event channel at Super-Kamiokande. Right panel: the time evolution of the Hardness ratio,  $R_{H/L}$ , for the electron neutrino- $^{40}\text{Ar}$  capture channel at DUNE.

distance between Earth and the CCSN to  $d = 10$  kpc.

Figure 7 shows the results for the total event rate for IBD in Super-Kamiokande on the left panel and the total event rate for  $\nu_e - ^{40}\text{Ar}$  capture in DUNE, on the right. Please note that because we chose to bin snapshots more closely near the onset and end of the CNO epoch, the inter-snapshot spacing of data points in Figure 7 is not necessarily equal to the integration time used to calculate the event rate, which is 50 ms. From the total event rates alone, it is clear that the onset of CNO can be detected through the divergent trends in the event rates of both experiments. When the Z9.6 simulation neutrino emission is modified by matter effects alone, the event rates for  $\nu_e$  and  $\bar{\nu}_e$  trend together after the passage of the neutronization burst. However, there is a clear divergence in the relative event rates for  $\nu_e$  vs  $\bar{\nu}_e$  when CNO is included, with a significant increase in  $\nu_e$  capture in LAr contemporaneous with a significant decrease in  $\bar{\nu}_e$  capture in inverse beta decay. This relative shift in the event rates continues for the entirety of the CNO epoch, before the total event rates in both experiments abruptly return to trending together at  $t_{\text{pb}} = 170$  ms. The total event rate in LAr does not show any significant difference between the ‘no halo’ and ‘with halo’ cases, while the total events received during the CNO epoch for Super-Kamiokande are reduced an addition 10% when including the halo in CNO calculations.

Of course, the total event rate omits all of the information contained in the energy distribution of the observed signals for our proxy detectors. We might also consider measures which are sensitive to the energy dependence of  $\nu_e$  and  $\bar{\nu}_e$  events. To this end we introduce the ‘Hardness Ratio,’  $R_{H/L}$ , which splits the event rates in each

detection channel into two bins with detected neutrino energies above and below a cutoff energy,  $E_C = 15$  MeV. This gives,

$$R_{H/L} = \frac{N_{|E>E_C}}{N_{|E<E_C}}, \quad (11)$$

with a distinct  $R_{H/L}$  for each detection channel from which we consider. Figure 8 shows the Hardness ratio for inverse beta decay detection at Super-Kamiokande on the left panel and the right panel shows the Hardness ratio for  $\nu_e - ^{40}\text{Ar}$  capture detection at DUNE.

Much like the total event rates during this epoch of the CCSN explosion, the spectral hardness of  $\nu_e$  and  $\bar{\nu}_e$  are expected to trend together during this period of the Z9.6 CCSN.  $R_{H/L}$  gradually increases for both detection channels as the proto-neutron star at the core of the explosion cools from neutrino emission, causing the spectra of all emitted neutrinos to stiffen. With the onset of CNO we see that again the behavior of simultaneously divergent trends, this time for in  $R_{H/L}$  in both detection channels. However, the shifts in the Hardness ratio are less statistically significant than the CNO induced shifts in the total event rate. Likewise, there is very little distinction between the ‘no halo’ and ‘with halo’ cases for the  $R_{H/L}$  ratio.

To restore as much of the shape information as possible to our predicted signals from the Z9.6 simulation, we have performed a basic  $\Delta\chi^2$  hypothesis test on the received event distributions (assuming a uniform  $\Delta E = 4$  MeV for energy bins between 0 – 60 MeV and 50 ms integrated observing time), taking the ‘no CNO’ case as the null hypothesis for each channel. This will give us a measure of

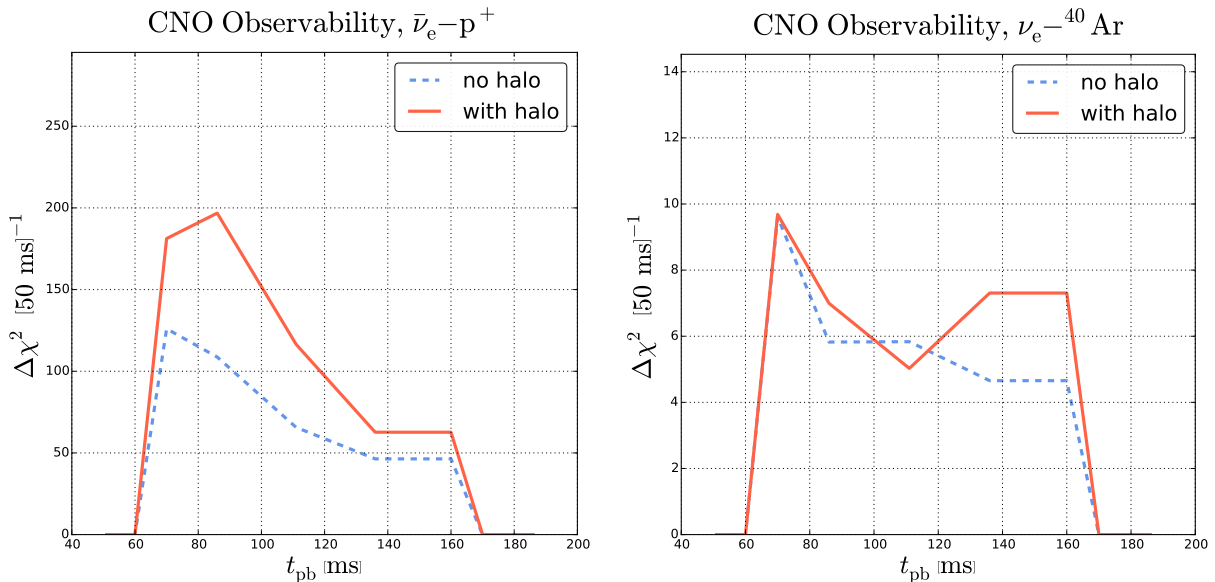


FIG. 9. Left panel: the time evolution of  $\Delta\chi^2$  for the inverse beta decay event channel at Super-Kamiokande. Right panel: the time evolution of  $\Delta\chi^2$ , for the  $\nu_e - {}^{40}\text{Ar}$  capture channel at DUNE. For both cases we take the absence of CNO to be the null hypothesis.

the raw statistical potential to extract information from the CNO epoch of the Z9.6 signal.

Shown in the left panel of Figure 9 are the results for the inverse beta decay channel in Super-Kamiokande and results for  $\nu_e - {}^{40}\text{Ar}$  capture detection at DUNE are shown in the right panel. These two figures illustrate the importance of including the halo neutrinos in CNO calculations. Typically, although not uniformly, CNO signals are more easily discriminated from non-CNO signals when halo neutrinos are accounted for in both Super-Kamiokande and DUNE. For the Z9.6 CCSN simulation, the effect is much more pronounced in Super-Kamiokande, where there is a  $\sim 60\%$  increase in  $\Delta\chi^2$  integrated over the CNO epoch. Although we do not attempt to make a detailed spectral reconstruction from the received signals in Super-Kamiokande and DUNE, both panels of Figure 9 taken together indicate that the spectral shape of the CNO signal is more easily discriminated from thermal neutrino emission when halo neutrinos are included in CNO calculation. Put another way, because previous studies have omitted halo neutrinos in their CNO calculations, their predictions for extracting meaningful signals from a supernova neutrino burst are likely to have been *overly pessimistic* with regard to strength of CNO signals.

The reason that the halo neutrinos tend to increase predictions of the CNO signal strength relative to calculations which omit halo neutrinos is straight forward. In the absence of coherently enhanced elastic scattering, the  $\nu - \nu$  contribution to Equation (2) is roughly  $\propto (R_\nu/r)^4$ . Because the elastic scattering which populates the halo spreads neutrinos out to trajectories which have wider intersection angles while conserving their overall numbers,

the  $\nu - \nu$  contribution to Equation (2) which includes the halo is softer than  $\propto (R_\nu/r)^4$ . This softening leads to a larger scale height for the  $\nu - \nu$  potential and results in moderately more adiabatic conditions for CNO. Increasing the adiabaticity of CNO leads to sharper spectral features in the neutrino energy distribution. An example of this can be seen clearly in the top panels of Figure 6, where the spectral swap between  $\nu_e - \nu_\gamma$  is greatly sharpened by the inclusion of the halo neutrinos in the CNO calculation.

#### IV. CONCLUSIONS

We have made the first multi-angle calculation of neutrino flavor evolution in the iron-core collapse supernova environment which includes the population of neutrinos scattered into the wide angle halo. We have shown that there are qualitative and quantitative consequences for resulting neutrino oscillation signatures, relative to CNO calculations which omit the halo neutrinos. We have shown that these changes have implications for the detectability of CNO in a CCSN neutrino burst signal.

The physical circumstances which proceed from the evolution of the explosion of the Z9.6 progenitor star produce an environment which is conducive to calculating CNO with the inclusion of halo neutrinos. Multi-angle suppression of neutrino flavor transformation deep within the envelope is present both prior to  $t_{\text{pb}} = 70$  ms and after  $t_{\text{pb}} = 170$  ms, while CNO is unsuppressed for the intervening 100 ms. That window of time coincides with the epoch of time wherein the explosion shock front has not yet grown outward to the initial radius of collective

neutrino flavor conversion. The relatively low radius of the shock creates a neutrino halo which is predominantly outward directed during the epoch of CNO, to the extent that the inward directed neutrino flux is found to be a sub-leading order contribution to the flavor changing Hamiltonian. This enables the multi-angle calculation of CNO for the outgoing flux of neutrinos during this window of time.

Comparing the results of our CNO calculations with those which omit the halo neutrino population, as well as those which omit CNO entirely, has yielded important results. Firstly, we find that the onset of the CNO epoch in the neutrino burst signal is clearly distinguishable from thermal emission. We also find that redistribution of neutrinos to wider emission trajectories via coherently enhanced neutral current nucleus scattering produces CNO evolution which is more adiabatic than one would predict when omitting the halo population. This changes the development of the spectral swap features which are hallmarks of CNO signals, reducing the effects of collective flavor oscillation decoherence, shifting spectral swap energies, and increasing the sharpness of swap transitions. Importantly, we find that detected CNO signals tend to be more clearly distinguished from thermal emission when including the halo neutrinos.

Looking forward we are hopeful for the detection of CNO signals from terrestrial neutrino detectors in the event of a galactic CCSN. Our results show that the neutrino halo, which is a generic phenomenon common to all CCSNe, tends to enhance the non-thermal features of

CNO signals, potentially rendering them more easily detectable. Conversely, this raises the possibility that previous studies which omit the presence of halo neutrinos in CNO may be overly pessimistic in their calculations of the detectability of CNO signals. While our study here is a narrow sampling of the potential variety of neutrino burst signals from CCSNe, it suggests that the observational opportunities for studying CCSNe through neutrino messengers is richer than previously imagined.

## ACKNOWLEDGMENTS

This work has been partly supported by Grant-in-Aid for Scientific Research (JP17H01130, JP17K14306, JP18H01212) from the Japan Society for Promotion of Science (JSPS) and the Ministry of Education, Science and Culture of Japan (MEXT, Nos. JP17H05206, JP17H06357, JP17H06364, JP24103001), and by the Central Research Institute of Stellar Explosive Phenomena (REISEP) at Fukuoka University and the associated projects (Nos. 171042,177103), and JICFuS as a priority issue to be tackled by using Post ‘K’ Computer. S.H. is supported by the U.S. Department of Energy under Award No. DE-SC0018327 and NSF Grants Nos. PHY-1908960 and PHY-1914409. Numerical computations were in part carried out on Cray XC50 at Center for Computational Astrophysics, National Astronomical Observatory of Japan.

- 
- [1] K. Langanke and G. Martínez-Pinedo, *Reviews of Modern Physics* **75**, 819 (2003).
- [2] A. Mezzacappa, *Annu. Rev. Nucl. Part. Sci.* **55**, 467 (2005).
- [3] S. Woosley and T. Janka, *Nature Physics* **1**, 147 (2005).
- [4] K. Kotake, K. Sato, and K. Takahashi, *Reports on Progress in Physics* **69**, 971 (2006).
- [5] H.-T. Janka, *Annu. Rev. Nucl. Part. Sci.* **62**, 407 (2012).
- [6] H.-T. Janka, “Neutrino Emission from Supernovae,” in *Handbook of Supernovae*, edited by A. W. Alsabti and P. Murdin (Springer International Publishing AG, 2017) p. 1575.
- [7] A. Burrows, *Reviews of Modern Physics* **85**, 245 (2013).
- [8] T. Foglizzo, R. Kazeroni, J. Guilet, F. Masset, M. González, B. K. Krueger, J. Novak, M. Oertel, J. Margueron, J. Faure, N. Martin, P. Blottiau, B. Peres, and G. Durand, *Pub. Astron. Soc. Aust.* **32**, e009 (2015).
- [9] K. Hirata, T. Kajita, M. Koshiba, M. Nakahata, Y. Oyama, N. Sato, A. Suzuki, M. Takita, Y. Totusuka, T. Kifune, T. Suda, K. Takahashi, T. Tanimori, K. Miyano, M. Yamada, E. W. Beier, L. R. Feldscher, S. B. Kim, A. K. Mann, F. M. Newcomer, R. van, W. Zhang, and B. G. Cortez, *Physical Review Letters* **58**, 1490 (1987).
- [10] R. M. Bionta, G. Blewitt, C. B. Bratton, D. Casper, A. Ciocio, R. Claus, B. Cortez, M. Crouch, S. T. Dye, S. Errede, G. W. Foster, W. Gajewski, K. S. Ganezer, M. Goldhaber, T. J. Haines, T. W. Jones, D. Kielczewska, W. R. Kropp, J. G. Learned, J. M. Losecco, J. Matthews, R. Miller, M. S. Mudan, H. S. Park, L. R. Price, F. Reines, J. Schultz, S. Seidel, E. Shumard, D. Sinclair, H. W. Sobel, J. L. Stone, L. R. Sulak, R. Svoboda, G. Thornton, J. C. van der Velde, and C. Wuest, *Physical Review Letters* **58**, 1494 (1987).
- [11] F. Vissani, *Journal of Physics G Nuclear Physics* **42**, 013001 (2015).
- [12] K. Scholberg, *Annual Review of Nuclear and Particle Science* **62**, 81 (2012).
- [13] S. Horiuchi and J. P. Kneller, *Journal of Physics G Nuclear Physics* **45**, 043002 (2018).
- [14] H. Duan, G. M. Fuller, and Y.-Z. Qian, *Annu. Rev. Nucl. Part. Sci.* **60**, 569 (2010).
- [15] A. Mirizzi, I. Tamborra, H.-T. Janka, N. Saviano, K. Scholberg, R. Bollig, L. Hüdepohl, and S. Chakraborty, *Nuovo Cimento Rivista Serie* **39**, 1 (2016).
- [16] S. Chakraborty, R. Hansen, I. Izaguirre, and G. Raffelt, *Nuclear Physics B* **908**, 366 (2016).
- [17] M. Tanabashi, K. Hagiwara, K. Hikasa, K. Nakamura, Y. Sumino, F. Takahashi, J. Tanaka, K. Agashe, G. Aielli, C. Amsler, and et al., *Phys. Rev. D* **98**, 030001 (2018).
- [18] L. Wolfenstein, *Phys. Rev. D* **17**, 2369 (1978).
- [19] S. P. Mikheyev and A. Y. Smirnov, *Yad. Fiz.* **42**, 1441

- (1985).
- [20] G. Fogli, E. Lisi, A. Marrone, and A. Mirizzi, *J. Cosmol. Astropart. Phys.* **12**, 010 (2007).
- [21] A. Esteban-Pretel, A. Mirizzi, S. Pastor, R. Tomàs, G. G. Raffelt, P. D. Serpico, and G. Sigl, *Phys. Rev. D* **78**, 085012 (2008).
- [22] S. Chakraborty, T. Fischer, A. Mirizzi, N. Saviano, and R. Tomàs, *Phys. Rev. Lett.* **107**, 151101 (2011).
- [23] S. Chakraborty, T. Fischer, A. Mirizzi, N. Saviano, and R. Tomàs, *Phys. Rev. D* **84**, 025002 (2011).
- [24] M.-R. Wu, Y.-Z. Qian, G. Martínez-Pinedo, T. Fischer, and L. Huther, *Phys. Rev. D* **91**, 065016 (2015).
- [25] M. Zaizen, T. Yoshida, K. Sumiyoshi, and H. Umeda, *Phys. Rev. D* **98**, 103020 (2018).
- [26] J. F. Cherry, J. Carlson, A. Friedland, G. M. Fuller, and A. Vlasenko, *Phys. Rev. Lett.* **108**, 261104 (2012).
- [27] J. F. Cherry, J. Carlson, A. Friedland, G. M. Fuller, and A. Vlasenko, *Phys. Rev. D* **87**, 085037 (2013).
- [28] V. Cirigliano, M. Paris, and S. Shalgar, *J. Cosmol. Astropart. Phys.* **11**, 019 (2018).
- [29] G. Raffelt, S. Sarikas, and D. d. S. Seixas, *Phys. Rev. Lett.* **111**, 091101 (2013).
- [30] A. Mirizzi, *Phys. Rev. D* **88**, 073004 (2013).
- [31] S. Chakraborty and A. Mirizzi, *Phys. Rev. D* **90**, 033004 (2014).
- [32] H. Duan and S. Shalgar, *Phys. Lett. B* **747**, 139 (2015).
- [33] B. Dasgupta and A. Mirizzi, *Phys. Rev. D* **92**, 125030 (2015).
- [34] S. Chakraborty, R. S. Hansen, I. Izaguirre, and G. G. Raffelt, *J. Cosmol. Astropart. Phys.* **1**, 028 (2016).
- [35] S. Chakraborty, R. S. Hansen, I. Izaguirre, and G. G. Raffelt, *J. Cosmol. Astropart. Phys.* **3**, 042 (2016).
- [36] B. Dasgupta, A. Mirizzi, and M. Sen, *J. Cosmol. Astropart. Phys.* **2**, 019 (2017).
- [37] S. Abbar and H. Duan, *Phys. Rev. D* **98**, 043014 (2018).
- [38] M. Delfan Azari, S. Yamada, T. Morinaga, W. Iwakami, H. Okawa, H. Nagakura, and K. Sumiyoshi, *Phys. Rev. D* **99**, 103011 (2019).
- [39] A. Heger and S. E. Woosley, *Astrophys. J.* **724**, 341 (2010).
- [40] T. Takiwaki and K. Kotake, *Mon. Not. R. Astron. Soc.* **475**, L91 (2018).
- [41] E. O’Connor, R. Bollig, A. Burrows, S. Couch, T. Fischer, H.-T. Janka, K. Kotake, E. J. Lentz, M. Liebendörfer, O. E. B. Messer, A. Mezzacappa, T. Takiwaki, and D. Vartanyan, *Journal of Physics G Nuclear Physics* **45**, 104001 (2018).
- [42] A. Mignone, *Journal of Computational Physics* **270**, 784 (2014).
- [43] E. F. Toro, M. Spruce, and W. Speares, *Shock Waves* **4**, 25 (1994).
- [44] J. M. Lattimer and F. Douglas Swesty, *Nucl. Phys. A* **535**, 331 (1991).
- [45] M. T. Keil, G. G. Raffelt, and H.-T. Janka, *Astrophys. J.* **590**, 971 (2003).
- [46] I. Tamborra, B. Müller, L. Hüdepohl, H.-T. Janka, and G. Raffelt, *Phys. Rev. D* **86**, 125031 (2012).
- [47] I. Tamborra, G. Raffelt, F. Hanke, H.-T. Janka, and B. Müller, *Phys. Rev. D* **90**, 045032 (2014).
- [48] H. Duan, G. M. Fuller, J. Carlson, and Y.-Z. Qian, *Phys. Rev. D* **74**, 105014 (2006).
- [49] B. Dasgupta and A. Dighe, *Phys. Rev. D* **77**, 113002 (2008).
- [50] Z. Maki, M. Nakagawa, and S. Sakata, *Prog. Theor. Phys.* **28**, 870 (1962).
- [51] A. Mirizzi and R. Tomàs, *Phys. Rev. D* **84**, 033013 (2011).
- [52] A. Friedland, *Physical Review Letters* **104**, 191102 (2010).
- [53] B. Dasgupta, A. Mirizzi, I. Tamborra, and R. Tomàs, *Phys. Rev. D* **81**, 093008 (2010).
- [54] S. A. Richers, G. C. McLaughlin, J. P. Kneller, and A. Vlasenko, *Phys. Rev. D* **99**, 123014 (2019).
- [55] COHERENT Collaboration, D. Akimov, J. B. Albert, P. An, C. Awe, P. S. Barbeau, B. Becker, V. Belov, A. Brown, A. Bolozdynya, B. Cabrera-Palmer, M. Cervantes, J. I. Collar, R. J. Cooper, R. L. Cooper, C. Cuesta, D. J. Dean, J. A. Detwiler, A. Eberhardt, Y. Efremenko, S. R. Elliott, E. M. Erkela, L. Fabris, M. Febraro, N. E. Fields, W. Fox, Z. Fu, A. Galindo-Uribarri, M. P. Green, M. Hai, M. R. Heath, S. Hedges, D. Hornback, T. W. Hossbach, E. B. Iverson, L. J. Kaufman, S. Ki, S. R. Klein, A. Khromov, A. Kononov, M. Kremer, A. Kumpan, C. Leadbetter, L. Li, W. Lu, K. Mann, D. M. Markoff, K. Miller, H. Moreno, P. E. Mueller, J. Newby, J. L. Orrell, C. T. Overman, D. S. Parno, S. Penttila, G. Perumpilly, H. Ray, J. Raybern, D. Reyna, G. C. Rich, D. Rimal, D. Rudik, K. Scholberg, B. J. Scholz, G. Sinev, W. M. Snow, V. Sosnovtsev, A. Shakirov, S. Suchyta, B. Suh, R. Tayloe, R. T. Thornton, I. Tolstukhin, J. Vanderwerp, R. L. Varner, C. J. Virtue, Z. Wan, J. Yoo, C.-H. Yu, A. Zawada, J. Zettlemoyer, A. M. Zderic, and aff13, *Science* **357**, 1123 (2017).
- [56] D. L. Tubbs and D. N. Schramm, *Astrophys. J.* **201**, 467 (1975).
- [57] S. M. Adams, C. S. Kochanek, J. F. Beacom, M. R. Vagins, and K. Z. Stanek, *Astrophys. J.* **778**, 164 (2013).
- [58] H. Duan, G. M. Fuller, J. Carlson, and Y.-Z. Qian, *Physical Review Letters* **97**, 241101 (2006).
- [59] “<http://www.phy.duke.edu/~schol/snowglobes/>”.